Realistic non-Gaussian-operation scheme in parity-detection-based Mach-Zehnder quantum interferometry

Chandan Kumar [1,*] Rishabh [2,†] and Shikhar Arora [1,‡]

[1]*Department of Physical Sciences, Indian Institute of Science Education and Research Mohali, Sector 81 SAS Nagar, Punjab 140306, India*
[2]*Department of Physics and Astronomy, University of Calgary, Calgary T2N1N4, Alberta, Canada*

We theoretically analyze phase sensitivity using a parity-detection-based Mach-Zehnder interferometer (MZI) with the input states generated by performing non-Gaussian operations, viz., photon subtraction, photon addition, and photon catalysis, on a two-mode squeezed vacuum (TMSV) state. Since these non-Gaussian operations are probabilistic, it is of utmost importance to take the success probability into account. To this end, we consider a realistic model of photon subtraction, addition, and catalysis and derive a single expression of the Wigner function for photon subtracted, added, and catalyzed TMSV states. The Wigner function is used to evaluate the lower bound on the phase sensitivity via quantum Cramér-Rao bound and parity-detection-based phase sensitivity in the MZI. We identify the ranges of squeezing and transmissivity parameters where the non-Gaussian states provide better phase sensitivity than the TMSV state. Taking the success probability into account, it turns out that the photon addition is the most advantageous among all three non-Gaussian operations. We hope that the generalized Wigner function derived in this paper will be useful in various quantum information protocols and state characterization.

I. INTRODUCTION

Quantum metrology strives to enhance measurement sensitivity by using quantum resources [1,2]. The canonical example of quantum metrology aims at improving the sensitivity of phase estimation by using a nonclassical field of light as input to the Mach-Zehnder interferometer (MZI). The phase sensitivity of the MZI can reach only up to the shot-noise limit (SNL) with solely a classical field of light [3]. On the other hand, with single-mode nonclassical states [4] and entangled states [5,6] as input to the MZI, the phase sensitivity can go beyond the SNL and reach the Heisenberg limit (HL) [7]. The HL has been reached in photon number parity measurement-based quantum interferometry [6,8–20], for instance, using NOON states as input [1,5,21]. However, the fragility of NOON states in the presence of photon loss limits their utility [14]. Phase sensitivity using a two-mode squeezed vacuum state (TMSV) can even exceed the HL [6]. However, the current experimental techniques pose a challenge to generate a strongly entangled TMSV state [22].

It has been shown that non-Gaussian operations such as photon subtraction, addition, and catalysis on the TMSV state can enhance the nonclassicality and entanglement content of the original state. These non-Gaussian states have been used in various protocols such as quantum teleportation [23–27], quantum key distribution [28–33], quantum illumination [34,35], and noiseless amplification [36] to enhance the

performance. With a similar vision, non-Gaussian states have also been considered as input to the MZI to further enhance the phase sensitivity [37–41].

These non-Gaussian operations are probabilistic, and therefore it is necessary to consider their success probability. However, the probabilistic nature of these operations has not been taken into account while studying the sensitivity of phase estimation, which can have a significant impact on resource utilization. This paper takes the success probability into account while analyzing the phase sensitivity and identifying the advantageous squeezing parameter and transmissivity region. To this end, we consider the practical model of photon subtraction, addition, and catalysis [42] and derive the generalized Wigner function describing the non-Gaussian two-mode squeezed vacuum (NGTMSV) states. The NGTMSV states include photon subtracted TMSV (PSTMSV), photon added TMSV (PATMSV), and photon catalyzed TMSV (PCTMSV) states. Hereafter, we use the term "non-Gaussian operations" (or "states") to refer to these three particular non-Gaussian operations (or states) until and unless specified otherwise. We use the generalized Wigner function of the NGTMSV state to calculate the quantum Fisher information (QFI) and phase sensitivity of the parity-detection-based MZI. We stress that, compared to Gaussian states, the investigation of these non-Gaussian states involves complicated calculations. Further, the realistic scheme adds an extra complication of transmissivity parameters corresponding to the beam splitters used in the implementation of these non-Gaussian operations, which significantly enhances the challenge for the theoretical analysis [42].

We analyze the theoretical lower bound on the phase sensitivity for the input NGTMSV states using the quantum

---
*chandan.quantum@gmail.com
†rishabh1@ucalgary.ca
‡shikhar.quantum@gmail.com

Cramér-Rao bound (QCRB). We then derive and study the phase sensitivity behavior for these states for parity-detection-based MZI. In order to compare the relative performance of the NGTMSV states and the TMSV state, we introduce a figure of merit defined as the difference between the phase sensitivity of these states. This figure of merit enables us to identify the advantageous squeezing and transmissivity parameter ranges. We also study the impact of the probabilistic nature of the non-Gaussian state generation on the phase sensitivity. Of the three non-Gaussian operations, the photon addition operation maximizes the product of probability and the difference between the phase sensitivity of the NGTMSV states and the TMSV state.

The derived Wigner functions for NGTMSV states, including PSTMSV, PATMSV, and PCTMSV states, will provide an impetus for dealing with various non-Gaussian continuous variable (CV) quantum information processing protocols that generally involve very complex analysis. Such expressions do not exist in the literature to the best of our knowledge. Our paper also furnishes a single expression of parity-detection-based phase sensitivity to cover all three non-Gaussian operations, including symmetric and asymmetric operations. States generated by ideal symmetric PS, ideal symmetric PA, and asymmetric PC operations on TMSV states have been considered as input to the parity-detection-based MZI [38,40,41] and form a special case of our general analysis. The figure of merit defined in this paper, along with the considerations involving the probability of non-Gaussian state generation, will allow experimentalists to choose suitable parameters to achieve higher phase sensitivity with resource optimization.

The paper is structured as follows. In Sec. II, we briefly describe the formalism of continuous variable systems. In Sec. III, we derive a general expression of the Wigner function of the NGTMSV state. Section IV contains the analysis of the lower bound of the phase sensitivity using QCRB. We then study the phase sensitivity using the parity-detection-based MZI. Finally, in Sec. V, we summarize our main results and discuss future prospects.

II. FORMALISM OF CV SYSTEMS

An n-mode quantum system is represented by n pairs of Hermitian operators $\hat{q}_i$, $\hat{p}_i$ ($i = 1, \ldots, n$) known as quadrature operators [43–47], which can be written in a column vector form as

$$\hat{\xi} = (\hat{\xi}_i) = (\hat{q}_1, \hat{p}_1 \ldots, \hat{q}_n, \hat{p}_n)^T, \quad i = 1, 2, \ldots, 2n. \quad (1)$$

The canonical commutation relations can be compactly written as ($\hbar = 1$)

$$[\hat{\xi}_i, \hat{\xi}_j] = i\Omega_{ij}, \quad (i, j = 1, 2, \ldots, 2n), \quad (2)$$

where Ω is the $2n \times 2n$ matrix given by

$$\Omega = \bigoplus_{k=1}^{n} \omega = \begin{pmatrix} \omega & & \\ & \ddots & \\ & & \omega \end{pmatrix}, \quad \omega = \begin{pmatrix} 0 & 1 \\ -1 & 0 \end{pmatrix}. \quad (3)$$

The quadrature operators are related to the annihilation and creation operators via the relation

$$\hat{a}_i = \frac{1}{\sqrt{2}}(\hat{q}_i + i\hat{p}_i), \quad \hat{a}_i^\dagger = \frac{1}{\sqrt{2}}(\hat{q}_i - i\hat{p}_i). \quad (4)$$

It is convenient to describe the CV system in phase-space formalism. The Wigner distribution for a quantum system with a density operator $\hat{\rho}$ is defined as

$$W(\boldsymbol{\xi}) = \int \frac{d^n \boldsymbol{q}'}{(2\pi)^n} \left\langle \boldsymbol{q} - \frac{1}{2}\boldsymbol{q}' \middle| \hat{\rho} \middle| \boldsymbol{q} + \frac{1}{2}\boldsymbol{q}' \right\rangle \exp(i\boldsymbol{q}'^T \cdot \boldsymbol{p}), \quad (5)$$

where $\boldsymbol{\xi} = (q_1, p_1, \ldots, q_n, p_n)^T \in \mathbb{R}^{2n}$, $\boldsymbol{q}' \in \mathbb{R}^n$, $\boldsymbol{q} = (q_1, q_2, \ldots, q_n)^T$, and $\boldsymbol{p} = (p_1, p_2, \ldots, p_n)^T$. The Wigner function can also be expressed as the average of displaced parity operator [48]:

$$W(\boldsymbol{\xi}) = \frac{1}{\pi^n} \text{Tr}[\hat{\rho} \, D(\boldsymbol{\xi}) \hat{\Pi} D^\dagger(\boldsymbol{\xi})], \quad (6)$$

where $\hat{\Pi} = \prod_{i=0}^{n} \exp(i\pi \hat{a}_i^\dagger \hat{a}_i)$ is the parity operator and $D(\boldsymbol{\xi}) = \exp[i\hat{\xi} \, \Omega \, \boldsymbol{\xi}]$ is the displacement operator. The first-order moments for an n mode system are defined as

$$\boldsymbol{d} = \langle \hat{\xi} \rangle = \text{Tr}[\hat{\rho}\hat{\xi}], \quad (7)$$

and the second-order moments can be written in the form of a real symmetric $2n \times 2n$ covariance matrix defined as

$$V = (V_{ij}) = \frac{1}{2}\langle\{\Delta\hat{\xi}_i, \Delta\hat{\xi}_j\}\rangle, \quad (8)$$

where $\Delta\hat{\xi}_i = \hat{\xi}_i - \langle\hat{\xi}_i\rangle$, and $\{,\}$ denotes the anticommutator.

A state with a Gaussian Wigner distribution is called a Gaussian state. For Gaussian states, the Wigner function (5) can be simplified to [46]

$$W(\boldsymbol{\xi}) = \frac{\exp[-(1/2)(\boldsymbol{\xi} - \boldsymbol{d})^T V^{-1}(\boldsymbol{\xi} - \boldsymbol{d})]}{(2\pi)^n \sqrt{\det V}}, \quad (9)$$

where $\boldsymbol{d}$ is the displacement and V denotes the covariance matrix of the Gaussian state.

Homogeneous symplectic transformations are linear transformations that preserve the canonical commutation relation (2). A phase change operation, single-mode squeezing operation, two-mode beam splitter operation, and two-mode squeezing operation are examples of symplectic transformations. For every homogeneous symplectic transformation S, there exists a corresponding infinite-dimensional unitary representation $\mathcal{U}(S)$ acting on the Hilbert space. Under such transformations, the density operator transforms as $\rho \rightarrow \mathcal{U}(S)\rho\,\mathcal{U}(S)^\dagger$. The corresponding transformation of the displacement vector $\boldsymbol{d}$, covariance matrix V, and Wigner function is given by [43]

$$\boldsymbol{d} \rightarrow S\boldsymbol{d}, \quad V \rightarrow SVS^T, \quad \text{and } W(\xi) \rightarrow W(S^{-1}\xi). \quad (10)$$

In this paper, we will consider non-Gaussian operations on TMSV states. A TMSV state is produced by the action of a two-mode squeezing transformation on two uncorrelated vacuum modes. It is a zero-centered state with the covariance matrix given by

$$V_{A_1 A_2} = S_{A_1 A_2}(r)\mathbb{1}_4 S_{A_1 A_2}(r)^T, \quad (11)$$

where $\mathbb{1}_4$ is the 4×4 identity matrix representing the covariance matrix of the two uncorrelated vacuum modes and
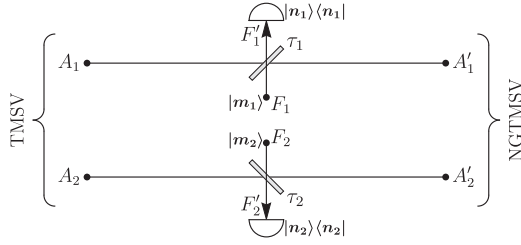
FIG. 1. Preparation scheme of the non-Gaussian TMSV state. The TMSV state is interfered with Fock states using beam splitters. Photon number resolving detectors given by the POVM $\{|n_1\rangle\langle n_1|, \mathbb{1} - |n_1\rangle\langle n_1|\}$ and $\{|n_2\rangle\langle n_2|, \mathbb{1} - |n_2\rangle\langle n_2|\}$ are applied to modes F_1' and F_2', respectively.

$S_{A_1A_2}(r)$ is the two-mode squeezing transformation given by

$$S_{A_1A_2}(r) = \begin{pmatrix} \cosh r\, \mathbb{1}_2 & \sinh r\, \mathbb{Z} \\ \sinh r\, \mathbb{Z} & \cosh r\, \mathbb{1}_2 \end{pmatrix}, \quad \mathbb{Z} = \begin{pmatrix} 1 & 0 \\ 0 & -1 \end{pmatrix}, \tag{12}$$

where r is the squeezing parameter. The Wigner function for the TMSV state can be readily computed using Eq. (9):

$$W(\xi) = \frac{1}{\pi^2} \exp\left[-\left(q_1^2 + p_1^2 + q_2^2 + p_2^2\right)\cosh(2r) \right.$$
$$\left. + 2(q_1q_2 - p_1p_2)\sinh(2r)\right]. \tag{13}$$

We shall now consider different non-Gaussian operations, viz., photon subtraction, addition, and catalysis, modeled via beam splitters on the TMSV state.

III. WIGNER FUNCTION OF THE NON-GAUSSIAN TWO-MODE SQUEEZED VACUUM STATE

The preparation scheme for the NGTMSV state is shown in Fig. 1. We interfere modes A_1 and A_2 of the TMSV state with ancillary modes F_1 and F_2, initiated to Fock states $|m_1\rangle$ and $|m_2\rangle$, using beam splitters of transmissivity τ_1 and τ_2, respectively. We represent the modes A_1 and A_2 by the quadrature operators $(\hat{q}_1, \hat{p}_1)^T$ and $(\hat{q}_2, \hat{p}_2)^T$ and the auxiliary modes F_1 and F_2 by the quadrature operators $(\hat{q}_3, \hat{p}_3)^T$ and $(\hat{q}_4, \hat{p}_4)^T$. The Wigner function for the four-mode system prior to the beam splitter transformations is given by

$$W_{F_1A_1A_2F_2}(\xi) = W_{A_1A_2}(\xi_1, \xi_2)W_{|m_1\rangle}(\xi_3)W_{|m_2\rangle}(\xi_4), \tag{14}$$

where $\xi_i = (q_i, p_i)^T$ $(i = 1, 2, 3, 4)$. We can evaluate the Wigner function of a Fock state $|n\rangle$ using Eq. (5) as

$$W_{|n\rangle}(q, p) = \frac{(-1)^n}{\pi} \exp(-q^2 - p^2) L_n[2(q^2 + p^2)]. \tag{15}$$

The two beam splitters $B(\tau_1, \tau_2) = B_{A_1F_1}(\tau_1) \oplus B_{A_2F_2}(\tau_2)$ act on the phase-space variables $(\xi_1, \xi_3, \xi_2, \xi_4)^T$, where the beam splitter operation $B_{A_kF_k}(\tau_k)$ acting on modes A_k and F_k is given by

$$B_{A_kF_k}(\tau_k) = \begin{pmatrix} \sqrt{\tau_k}\, \mathbb{1} & \sqrt{1-\tau_k}\, \mathbb{1} \\ -\sqrt{1-\tau_k}\, \mathbb{1} & \sqrt{\tau_k}\, \mathbb{1} \end{pmatrix}, \quad (k = 1, 2). \tag{16}$$

The transformed Wigner function is given by

$$W_{F_1'A_1'A_2'F_2'}(\xi) = W_{F_1A_1A_2F_2}[B(\tau_1, \tau_2)^{-1}\xi]. \tag{17}$$

The modes F_1' and F_2' are measured using photon number resolving detectors, given by the positive operator-valued measure (POVM) $\{\Pi_{n_1} = |n_1\rangle\langle n_1|, \mathbb{1} - \Pi_{n_1}\}$ and $\{\Pi_{n_2} = |n_2\rangle\langle n_2|, \mathbb{1} - \Pi_{n_2}\}$, respectively. The simultaneous click of the POVM elements Π_{n_1} and Π_{n_2} heralds successful non-Gaussian operations on both the modes. The corresponding un-normalized Wigner function is given by

$$\widetilde{W}^{\mathrm{NG}}_{A_1'A_2'}(\xi_1, \xi_2) = (2\pi)^2 \int d^2\xi_3 d^2\xi_4 \underbrace{W_{F_1'A_1'A_2'F_2'}(\xi_1, \xi_2, \xi_3, \xi_4)}_{\text{Four-mode entangled state}}$$
$$\times \underbrace{W_{|n_1\rangle}(\xi_3)}_{\text{Projection on } |n_1\rangle\langle n_1|} \underbrace{W_{|n_2\rangle}(\xi_4)}_{\text{Projection on } |n_2\rangle\langle n_2|}. \tag{18}$$

By choosing suitable values of (m_i, n_i), we can perform three different non-Gaussian operations on mode A_i as follows: (i) photon subtraction for $m_i < n_i$, (ii) photon addition for $m_i > n_i$, and (iii) photon catalysis for $m_i = n_i$.

The action of photon subtraction, photon addition, and photon catalysis on TMSV states yields PSTMSV, PATMSV, and PCTMSV states, respectively, which are non-Gaussian states. However, zero-photon catalysis, corresponding to $m_i = n_i = 0$ is a Gaussian operation, and therefore the resulting state, the zero-photon catalyzed TMSV state, is a Gaussian state.

In this paper, we consider both asymmetric and symmetric non-Gaussian operations on the TMSV state, which can be obtained by putting suitable conditions on parameters m_i, n_i, and τ_i, as shown in Table I. It should be noted that the asymmetric non-Gaussian operations are performed on mode A_2 of the TMSV state.

Equation (18) can be converted into a Gaussian integral using the generating function for the Laguerre polynomial appearing in the Wigner function of the Fock state (15):

$$L_n[2(q^2 + p^2)] = \widehat{D} \exp\left[\frac{st}{2} + s(q + ip) - t(q - ip)\right], \tag{19}$$

with

$$\widehat{D} = \frac{2^n}{n!} \frac{\partial^n}{\partial s^n} \frac{\partial^n}{\partial t^n} \{\bullet\}_{s=t=0}. \tag{20}$$

Integration of Eq. (18) yields

$$\widetilde{W}^{\mathrm{NG}}_{A_1'A_2'} = \frac{1}{a_0\pi^2} \widehat{D}_1 \exp(\boldsymbol{\xi}^T M_1 \boldsymbol{\xi} + \boldsymbol{u}^T M_2 \boldsymbol{\xi} + \boldsymbol{u}^T M_3 \boldsymbol{u}), \tag{21}$$

where $a_0 = 1 + \alpha^2(1 - \tau_1\tau_2)$, column vectors $\boldsymbol{\xi}$ and $\boldsymbol{u}$ are defined as

$$\boldsymbol{\xi} = (q_1, p_1, q_2, p_2)^T,$$
$$\boldsymbol{u} = (u_1, v_1, u_2, v_2, u_1', v_1', u_2', v_2')^T, \tag{22}$$

and differential operator $\widehat{D}_1$ is defined as

$$\widehat{D}_1 = \frac{(-2)^{m_1+m_2+n_1+n_2}}{m_1! m_2! n_1! n_2!} \frac{\partial^{m_1}}{\partial u_1^{m_1}} \frac{\partial^{m_1}}{\partial v_1^{m_1}} \frac{\partial^{m_2}}{\partial u_2^{m_2}} \frac{\partial^{m_2}}{\partial v_2^{m_2}}$$
$$\times \frac{\partial^{n_1}}{\partial u_1'^{m_1}} \frac{\partial^{n_1}}{\partial v_1'^{m_1}} \frac{\partial^{n_2}}{\partial u_2'^{m_2}} \frac{\partial^{n_2}}{\partial v_2'^{m_2}} \{\bullet\}_{\substack{u_1=v_1=u_2=v_2=0 \\ u_1'=v_1'=u_2'=v_2'=0}}. \tag{23}$$

TABLE I. Conditions on the number of input photons m_i and detected photons n_i and the transmissivity τ_i of the beam splitters for various asymmetric and symmetric non-Gaussian operations on the TMSV state.

Operations	Input		Detected		Transmissivity	
	m_1	m_2	n_1	n_2	τ_1	τ_2
Asym n-PS	0	0	0	n	1	τ
Asym n-PA	0	n	0	0		
Asym n-PC	0	n	0	n		
Sym n-PS	0	0	n	n	τ	τ
Sym n-PA	n	n	0	0		
Sym n-PC	n	n	n	n		

Further, the explicit form of the matrices M_1, M_2, and M_3 are provided in Eqs. (A1), (A2), and (A3) of Appendix A. The probability of n_1 and n_2 photon detection on mode F_1' and F_2', respectively, can be evaluated as

$$P^{\mathrm{NG}} = \int d^2\xi_1 d^2\xi_2 \widetilde{W}^{\mathrm{NG}}_{A_1'A_2'}(\xi_1,\xi_2)$$
$$= a_0^{-1}\widehat{\boldsymbol{D}_1}\exp(\boldsymbol{u}^T M_4 \boldsymbol{u}), \qquad (24)$$

where the matrix M_4 is given in Eq. (B1) of Appendix B. Figure 2 shows the success probability of various non-Gaussian operations, which is the same as the probability of detecting n_1 and n_2 photons on modes A_1 and A_2, as a function of the transmissivity τ and squeezing parameter $\lambda =$

$\tanh r$. We notice a vertical band of high success probability for asymmetric photon subtraction for intermediate squeezing values and all transmissivity values. In contrast, for symmetric photon subtraction, the region of high success probability occurs only for low transmissivity and intermediate values of squeezing. On the other hand, for photon addition, the success probability is high for low transmissivity and small squeezing. In contrast, we notice a horizontal band of high success probability for high transmissivity values and all squeezing values for photon catalysis. Interestingly, in the limit $\tau \to 1$, the incoming photon is detected with unit probability, and therefore the success probability for photon catalysis approaches unity. However, the resulting state is the same as the input TMSV state, and therefore no catalysis operation takes place.
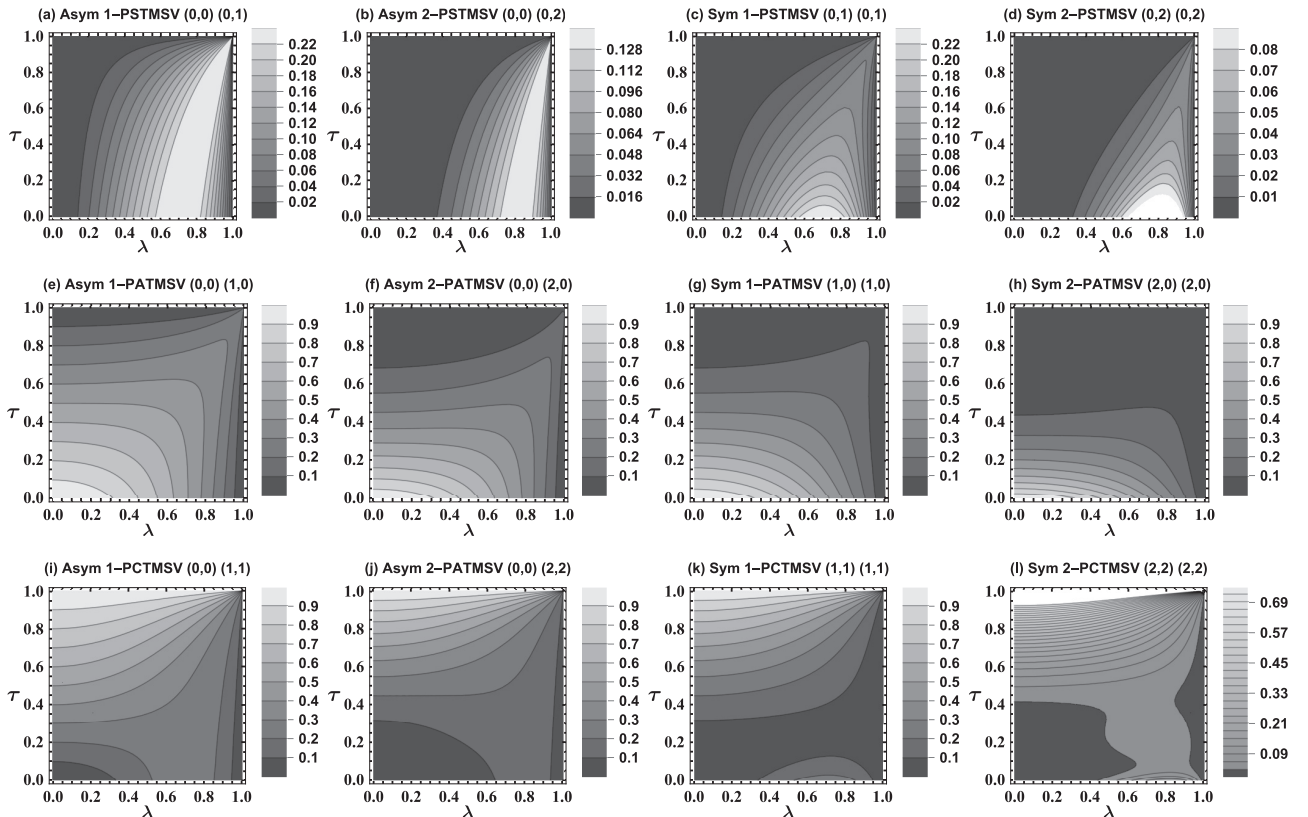

FIG. 2. The probability P^{NG} of detecting n_1 and n_2 photons on modes A_1 and A_2 as a function of the transmissivity τ and squeezing parameter λ. For symmetric non-Gaussian operations, we have set $\tau_1 = \tau_2 = \tau$. For asymmetric non-Gaussian operations, $\tau_1 = 1$ and $\tau_2 = \tau$. The value of $(m_1, n_1)(m_2, n_2)$ for each panel is also shown. Both the vertical and horizontal axes are dimensionless.

Of all the three non-Gaussian operations, photon subtraction occurs with relatively low probability compared to photon addition and catalysis. We notice two general trends.

(i) Success probability of non-Gaussian operations on both the modes is less as compared to non-Gaussian operations on one of the modes.

(ii) Success probability decreases for higher photon number detection.

The normalized Wigner function $W_{A_1'A_2'}^{NG}$ of the NGTMSV state turns out to be

$$W_{A_1'A_2'}^{NG}(\xi_1, \xi_2) = (P^{NG})^{-1} \widetilde{W}_{A_1'A_2'}^{NG}(\xi_1, \xi_2). \quad (25)$$

We can easily obtain several special cases from the above-derived Wigner function of the NGTMSV state. For instance, the Wigner function of the ideal PSTMSV state $\hat{a}_1^{n_1} \hat{a}_2^{n_2} |TMSV\rangle$ can be obtained by setting $\tau_1 = \tau_2 = 1$ in the symmetric photon subtraction case. Similarly, the Wigner function of the ideal PATMSV state $\hat{a}_1^{\dagger m_1} \hat{a}_2^{\dagger m_2} |TMSV\rangle$ can be obtained by setting $\tau_1 = \tau_2 = 1$ in the symmetric photon addition case.

We can calculate the average of Weyl (symmetrically) ordered operators using the Wigner function as follows:

$$\langle \vdots \hat{q}_1^{a_1} \hat{p}_1^{b_1} \hat{q}_2^{a_2} \hat{p}_2^{b_2} \vdots \rangle = \int d^4\xi \, q_1^{a_1} p_1^{b_1} q_2^{a_2} p_2^{b_2} W_{A_1'A_2'}^{NG}(\xi), \quad (26)$$

where the symbol $\vdots \bullet \vdots$ represents Weyl ordering. This quantity, akin to the moment generating function, can be evaluated using parametric differentiation technique as follows:

$$\mathcal{M}_{a_1,b_1}^{a_2,b_2} = \widehat{D_2} \int d^4\xi \, e^{x_1 q_1 + y_1 p_1 + x_2 q_2 + y_2 p_2} W_{A_1'A_2'}^{NG}(\xi), \quad (27)$$

with

$$\widehat{D_2} = \frac{\partial^{a_1}}{\partial x_1^{a_1}} \frac{\partial^{b_1}}{\partial y_2^{b_2}} \frac{\partial^{a_2}}{\partial x_2^{a_2}} \frac{\partial^{b_2}}{\partial y_2^{b_2}} \{\bullet\}_{x_1=y_1=x_2=y_2=0}. \quad (28)$$

On integrating Eq. (27), we obtain

$$\mathcal{M}_{a_1,b_1}^{a_2,b_2} = \frac{\widehat{D_2}\widehat{D_1} \exp\left(\boldsymbol{u}^T M_4 \boldsymbol{u} + \boldsymbol{u}^T M_5 \boldsymbol{x} + \boldsymbol{x}^T M_6 \boldsymbol{x}\right)}{\widehat{D_1} \exp\left(\boldsymbol{u}^T M_4 \boldsymbol{u}\right)}, \quad (29)$$

where $\boldsymbol{x} = (x_1, y_1, x_2, y_2)^T$ is a column vector, and the explicit forms of matrices M_5 and M_6 are provided in Eqs. (C1) and (C2) of Appendix C.

IV. PHASE ESTIMATION WITH THE NGTMSV STATE VIA MZI

We consider a balanced MZI consisting of two $50:50$ beam splitters and two phase shifters, as depicted in Fig. 3. The two input modes are denoted by the annihilation operators $\hat{a}_1$ and $\hat{a}_2$. The input to the interferometer is NGTMSV states, including PSTMSV, PATMSV, and PCTMSV states. It should be noted that the cases corresponding to unsuccessful non-Gaussian operations are discarded. Here we use the well-known Schwinger representation of SU(2) algebra to describe the transformation of a beam splitter [49]. The generators of the SU(2) algebra can be described using the two sets of Bose
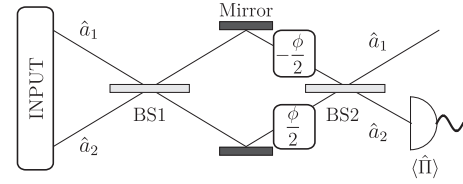

FIG. 3. Schematic of the Mach-Zehnder interferometer for the phase-shift detection.

operators as

$$\hat{J}_1 = \frac{1}{2}(\hat{a}_1^\dagger \hat{a}_2 + \hat{a}_1 \hat{a}_2^\dagger),$$
$$\hat{J}_2 = \frac{1}{2i}(\hat{a}_1^\dagger \hat{a}_2 - \hat{a}_1 \hat{a}_2^\dagger), \quad (30)$$
$$\hat{J}_3 = \frac{1}{2}(\hat{a}_1^\dagger \hat{a}_1 - \hat{a}_2^\dagger \hat{a}_2),$$

which satisfy the commutation relations $[J_i, J_j] = i\epsilon_{ijk}J_k$. While the actions of the first and the second balanced beam splitters are given by $e^{-i(\pi/2)J_1}$ and $e^{i(\pi/2)J_1}$, the collective action of the two phase shifters is given by $e^{i\phi J_3}$. Therefore, the infinite-dimensional unitary transformation corresponding to the balanced MZI can be written as

$$\mathcal{U}(S_{MZI}) = e^{-i(\pi/2)J_1} e^{i\phi J_3} e^{i(\pi/2)J_1} = e^{-i\phi J_2}, \quad (31)$$

where ϕ is the unknown phase to be estimated. The corresponding symplectic transformation S_{MZI} acting on the phase-space variables $(\xi_1, \xi_2)^T$ is given by

$$S_{MZI} = \begin{pmatrix} \cos(\phi/2)\mathbb{1} & -\sin(\phi/2)\mathbb{1} \\ \sin(\phi/2)\mathbb{1} & \cos(\phi/2)\mathbb{1} \end{pmatrix}. \quad (32)$$

Therefore, the input Wigner function transforms as follows under the action of S_{MZI}:

$$W_{in}(\xi) \rightarrow W_{in}\left(S_{MZI}^{-1}\xi\right) = W_{out}(\xi). \quad (33)$$

A. Quantum Fisher information

Although we will be using parity detection to estimate the phase, QCRB provides a useful lower bound of the phase sensitivity. This lower bound of phase sensitivity is given by [50]

$$\Delta\phi_{min} = \frac{1}{\sqrt{F_Q}}, \quad (34)$$

where F_Q is QFI. It is independent of the type of measurement performed and depends solely on the input state. The phase shifts are defined with respect to an external reference beam [51]. It can be calculated for a pure state as follows:

$$F_Q = 4[\langle \psi'|\psi'\rangle - |\langle \psi'|\psi\rangle|^2], \quad (35)$$

where $|\psi\rangle = e^{i\phi J_3} e^{i\pi J_1/2}|in\rangle$ is the quantum state prior to the second beam splitter and $|\psi'\rangle = \partial|\psi\rangle/\partial\phi$. The QFI can also be written in terms of the input state as

$$F_Q = 4[\langle in|\hat{J}_2^2|in\rangle - |\langle in|\hat{J}_2|in\rangle|^2]. \quad (36)$$

To evaluate the QFI using the moment generating function (29), we write $\hat{J}_2$ and $\hat{J}_2^2$ in terms of the quadrature operators and symmetrize them. The operator

$$\hat{J}_2 = \frac{1}{2}(\hat{q}_1 \hat{p}_2 - \hat{p}_1 \hat{q}_2) \quad (37)$$

is already symmetric in the quadrature operators. We note that for the NGTMSV states, $\langle \text{in}|\hat{J}_2|\text{in}\rangle$ evaluates to zero. The operator $\hat{J}_2^2$ can be written as

$$\hat{J}_2^2 = \frac{1}{4}\left(\hat{q}_1^2\hat{p}_2^2 + \hat{p}_1^2\hat{q}_2^2 - \hat{q}_1\hat{p}_1\hat{p}_2\hat{q}_2 - \hat{p}_1\hat{q}_1\hat{q}_2\hat{p}_2\right). \quad (38)$$

On symmetrizing $\hat{J}_2^2$, we get

$$\hat{J}_2^2 = \frac{1}{4}\left[\hat{q}_1^2\hat{p}_2^2 + \hat{p}_1^2\hat{q}_2^2 \right.$$
$$- \frac{(\hat{q}_1\hat{p}_1 + \hat{p}_1\hat{q}_1 + i)}{2}\frac{(\hat{p}_2\hat{q}_2 + \hat{q}_2\hat{p}_2 - i)}{2}$$
$$\left. - \frac{(\hat{q}_1\hat{p}_1 + \hat{p}_1\hat{q}_1 - i)}{2}\frac{(\hat{p}_2\hat{q}_2 + \hat{q}_2\hat{p}_2 + i)}{2}\right]. \quad (39)$$

Therefore, the QFI (36) can be written as

$$F_Q = -\frac{1}{8} + \frac{1}{4}\langle\hat{q}_1^2\hat{p}_2^2\rangle + \frac{1}{4}\langle\hat{p}_1^2\hat{q}_2^2\rangle - \frac{1}{2}\langle\vdots\hat{q}_1\hat{p}_1\hat{q}_2\hat{p}_2\vdots\rangle. \quad (40)$$

This can be easily evaluated using the moment generating function (29) as

$$F_Q = -\frac{1}{8} + \frac{1}{4}\mathcal{M}_{2,0}^{0,2} + \frac{1}{4}\mathcal{M}_{0,2}^{2,0} - \frac{1}{2}\mathcal{M}_{1,1}^{1,1}. \quad (41)$$

We first analyze the effect of squeezing on $\Delta\phi_{\min}$, while the transmissivity is kept fixed. We plot $\Delta\phi_{\min}$ as a function of squeezing in Fig. 4.

The results show that $\Delta\phi_{\min}$ for NGTMSV states can achieve a lower value as compared to the TMSV state. Among all the three non-Gaussian operations, symmetric photon addition attains the minimum value of $\Delta\phi_{\min}$. Since the expressions for $\Delta\phi_{\min}$ corresponding to the Asym n-PSTMSV and Asym n-PATMSV states are the same, they yield the same results as can be seen in the plots. Within asymmetric operations, $\Delta\phi_{\min}$ achieves a lower value for higher photon number detection, and the same is true for symmetric non-Gaussian operations. However, as noticed in the previous section, the probability decreases for higher photon number detection. We now analyze the effect of transmissivity on $\Delta\phi_{\min}$ while keeping the squeezing fixed. The result is shown in Fig. 5. For photon subtraction and addition operations, $\Delta\phi_{\min}$ is minimized in the limit $\tau \to 1$, while for photon catalysis, $\Delta\phi_{\min}$ is minimized in the limit $\tau \to 0$. However, the probability for photon subtraction and addition approaches zero, in the limit $\tau \to 1$, and the probability of photon catalysis is low in the limit $\tau \to 0$. Again we observe that $\Delta\phi_{\min}$ achieves a lower value for higher photon number detection in the case of both asymmetric and symmetric photon addition and subtraction. However, this is only true in the low transmissivity regime for photon catalysis.

B. Parity-detection-based phase sensitivity

In this paper, we measure the photon number parity operator on the output mode $\hat{a}_2$ to estimate the phase. The corresponding photon number parity operator is given by

$$\hat{\Pi}_{\hat{a}_2} = \exp(i\pi\hat{a}_2^\dagger\hat{a}_2) = (-1)^{\hat{a}_2^\dagger\hat{a}_2}. \quad (42)$$

This measurement differentiates between odd and even numbers of photons. The expectation value of the parity operator can be written in terms of the Wigner function using Eq. (6)
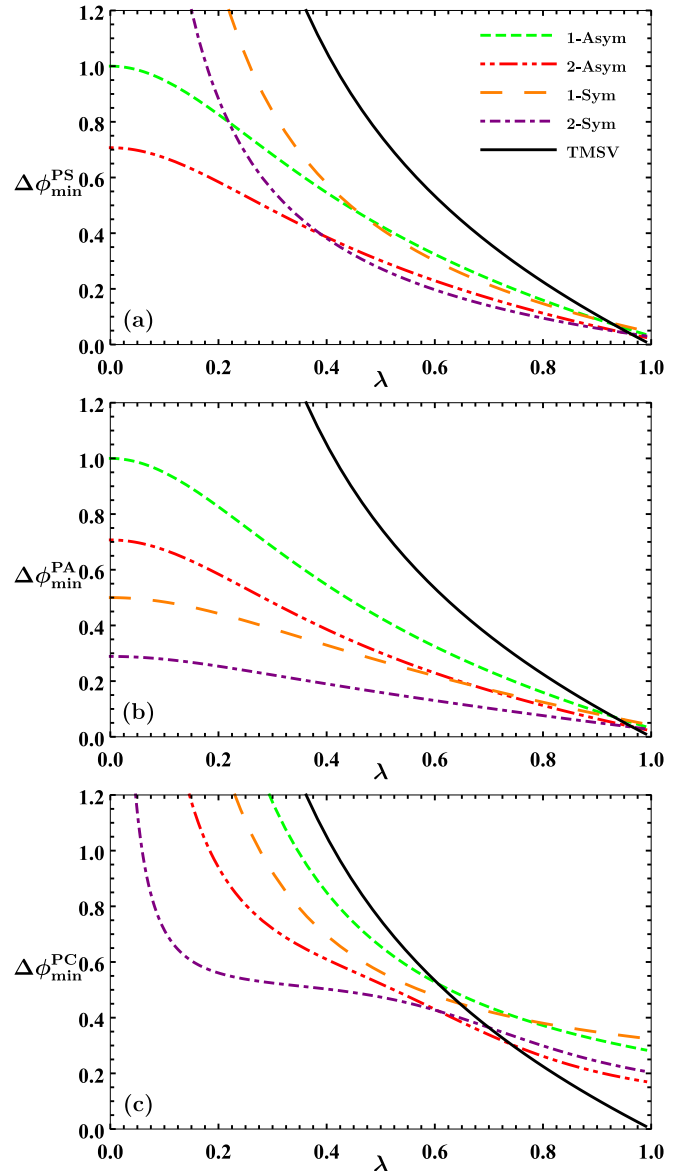

FIG. 4. The minimum phase uncertainty $\Delta\phi_{\min}$ obtained from the quantum Cramér-Rao bound, for NGTMSV states, as a function of the squeezing parameter λ. The value of transmissivity has been taken as $\tau = 0.9$ for panels (a) and (b) and $\tau = 0.2$ for panel (c). The vertical axis is in rad, while the horizontal axis is dimensionless.

as [52]

$$\langle\hat{\Pi}_{\hat{a}_2}\rangle = f(\phi) = \pi\int d^2\xi_1\, W_{\text{out}}(\xi_1, 0). \quad (43)$$

Using the Wigner function of the input NGTMSV state (25), the average of the parity operator evaluates to

$$f(\phi) = \frac{a_0\,\widehat{\boldsymbol{D}}_1\exp(\boldsymbol{u}^T M_7\boldsymbol{u})}{b_0\,\widehat{\boldsymbol{D}}_1\exp(\boldsymbol{u}^T M_4\boldsymbol{u})}, \quad (44)$$

where $b_0 = (1 - \lambda^2)^{-1}\sqrt{1 + \lambda^2\tau_1\tau_2[\lambda^2\tau_1\tau_2 + 2\cos(2\phi)]}$ and the explicit form of matrix M_7 is provided in Eq. (D1) of Appendix D.
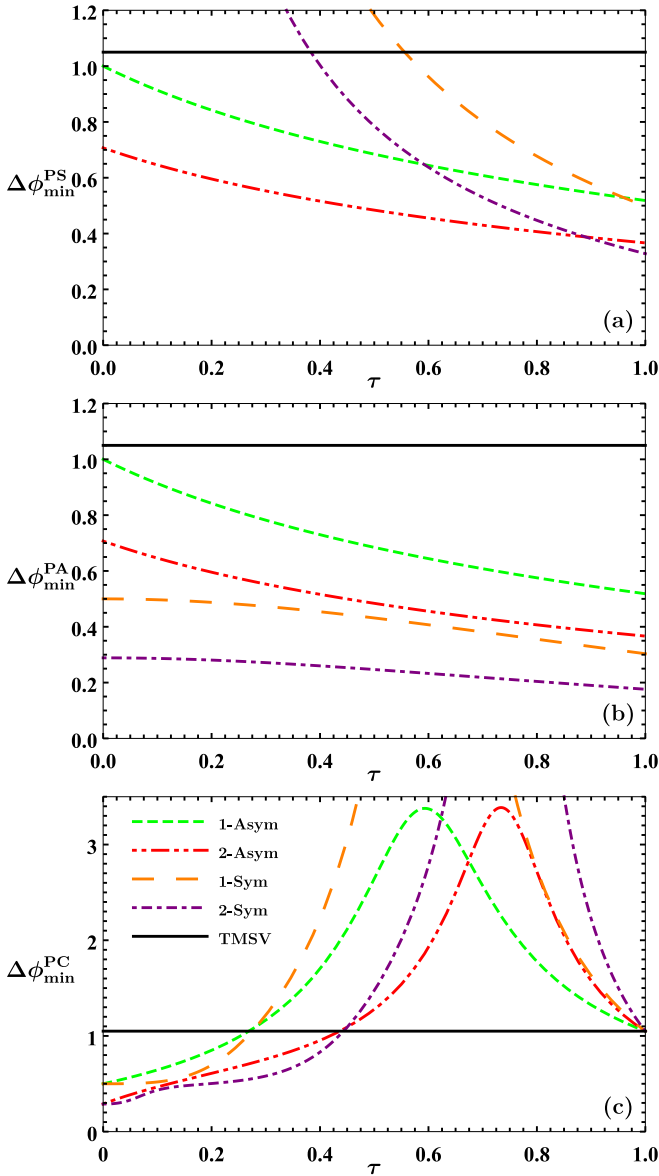
FIG. 5. The minimum phase uncertainty $\Delta\phi_{\min}$ obtained from the quantum Cramér-Rao bound, for NGTMSV states, as a function of transmissivity τ. The value of squeezing parameter has been set as $\lambda = 0.4$. The vertical axis is in rad, while the horizontal axis is dimensionless.
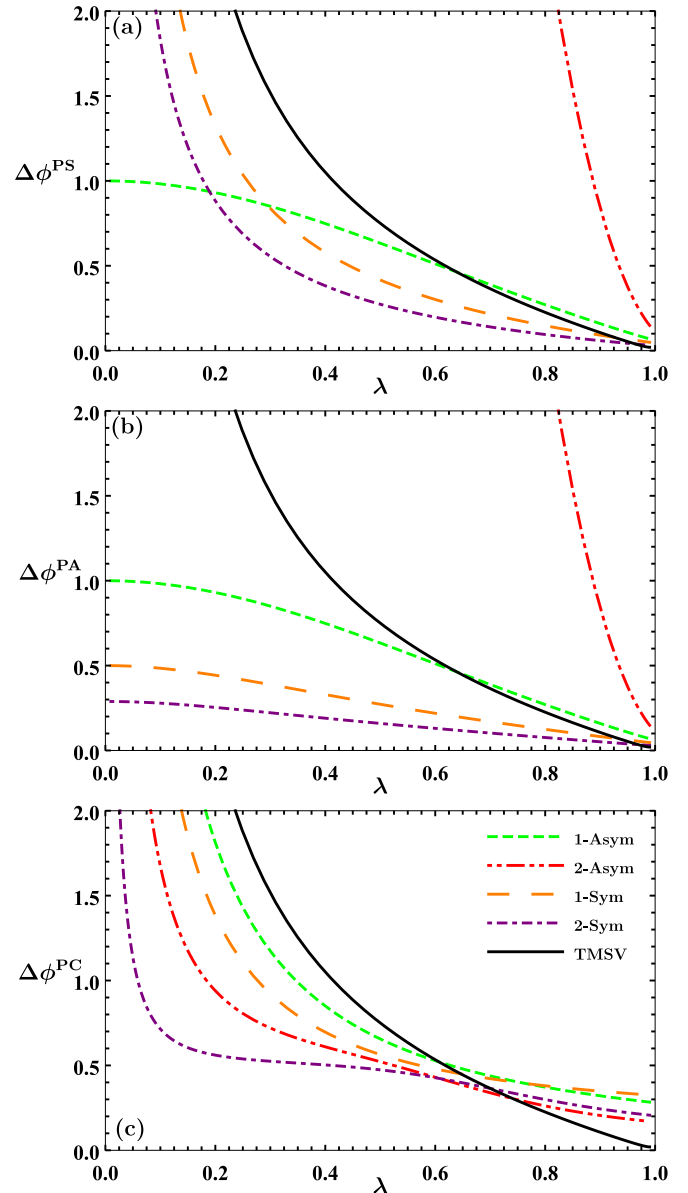

FIG. 6. Phase uncertainty $\Delta\phi$ for NGTMSV states, as a function of the squeezing parameter λ. The value of transmissivity has been taken as $\tau = 0.9$ for panels (a) and (b) and $\tau = 0.2$ for panel (c), while phase has been set as $\phi = 0.01$ rad for all the cases. The vertical axis is in rad, while the horizontal axis is dimensionless.

The phase uncertainty or sensitivity can be obtained using the error propagation formula as

$$\Delta\phi = \frac{\sqrt{1 - f(\phi + \pi/2)^2}}{|\partial f(\phi + \pi/2)/\partial\phi|}. \tag{45}$$

We now numerically investigate the dependence of $\Delta\phi$ on squeezing, transmissivity, and phase magnitude. First, we plot $\Delta\phi$ as a function of squeezing while keeping the transmissivity and phase constant. The result is shown in Fig. 6. Symmetric photon subtraction and addition perform better than the TMSV state for almost the whole range of squeezing, but the relative performance compared to the TMSV state becomes worse as λ approaches 1. Among asymmetric cases, single-photon subtraction and addition yield better phase sen-

sitivity only up to a certain threshold squeezing above which the TMSV state performs better. Similar behavior is also observed for all symmetric and asymmetric photon catalysis cases.

We also notice a few similarities between Figs. 4 and 6.

(i) The qualitative behaviors for different non-Gaussian operations are identical except for asymmetric subtraction and addition operations.

(ii) The performance of symmetric photon addition is the best among all the non-Gaussian operations.

(iii) The relative performance of NGTMSV states as compared to the TMSV state enhances for small values of squeezing.
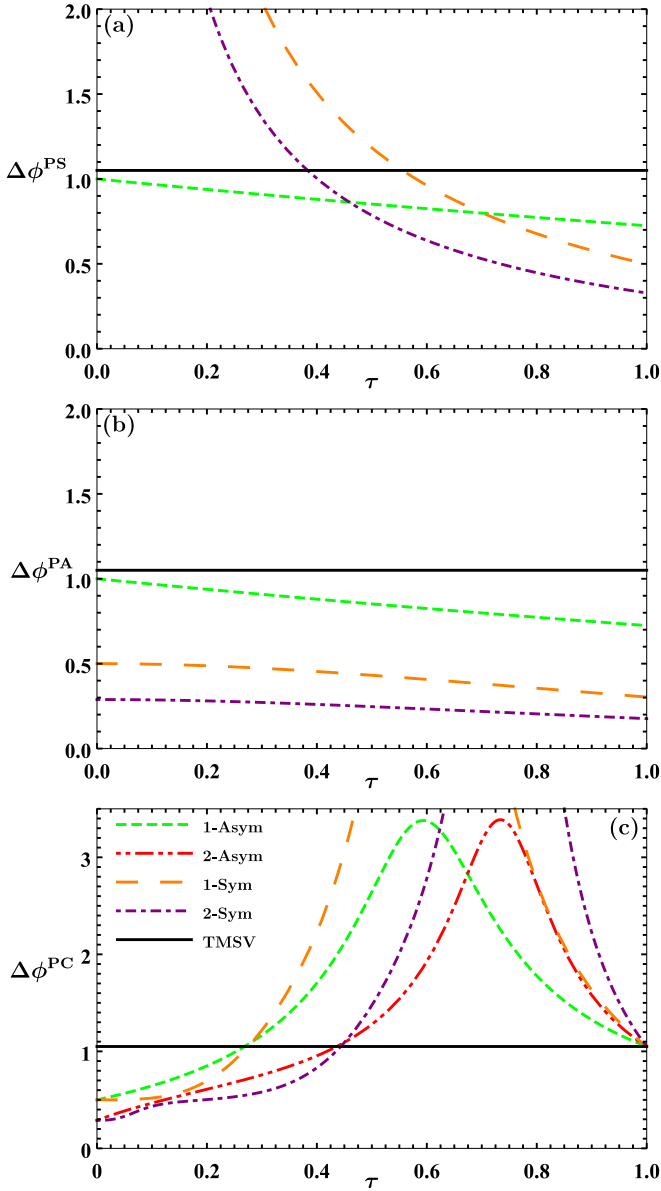
FIG. 7. Phase uncertainty $\Delta\phi$ for NGTMSV states, as a function of the beam splitter transmissivity τ. The parameters have been set as $\lambda = 0.4$ and $\phi = 0.01$ rad for all the cases. The vertical axis is in rad, while the horizontal axis is dimensionless.

FIG. 8. Phase uncertainty $\Delta\phi$ for NGTMSV states, as a function of the phase ϕ. The value of transmissivity has been taken as $\tau = 0.9$ for panels (a) and (b) and $\tau = 0.2$ for panel (c), while the squeezing parameter has been set as $\lambda = 0.4$ for all the cases. Both the vertical and horizontal axes are in rad.

(iv) Both $\Delta\phi_{\min}$ and $\Delta\phi$ achieve lower values for higher photon number detection in the case of asymmetric and symmetric non-Gaussian operations except for asymmetric photon subtraction and addition.

We note that Asym 2-PSTMSV and Asym 2-PATMSV states never yield phase sensitivity better than the TMSV state. We now plot $\Delta\phi$ as a function of transmissivity for fixed squeezing and phase in Fig. 7. As can be seen in Fig. 5, $\Delta\phi$ is minimized in the limit $\tau \rightarrow 1$ for photon subtraction and addition operations, while for photon catalysis, $\Delta\phi$ is minimized in the limit $\tau \rightarrow 0$. The qualitative behavior for different non-Gaussian operations is also similar to Fig. 5 except for the cases of Asym 2-PSTMSV and Asym 2-PATMSV
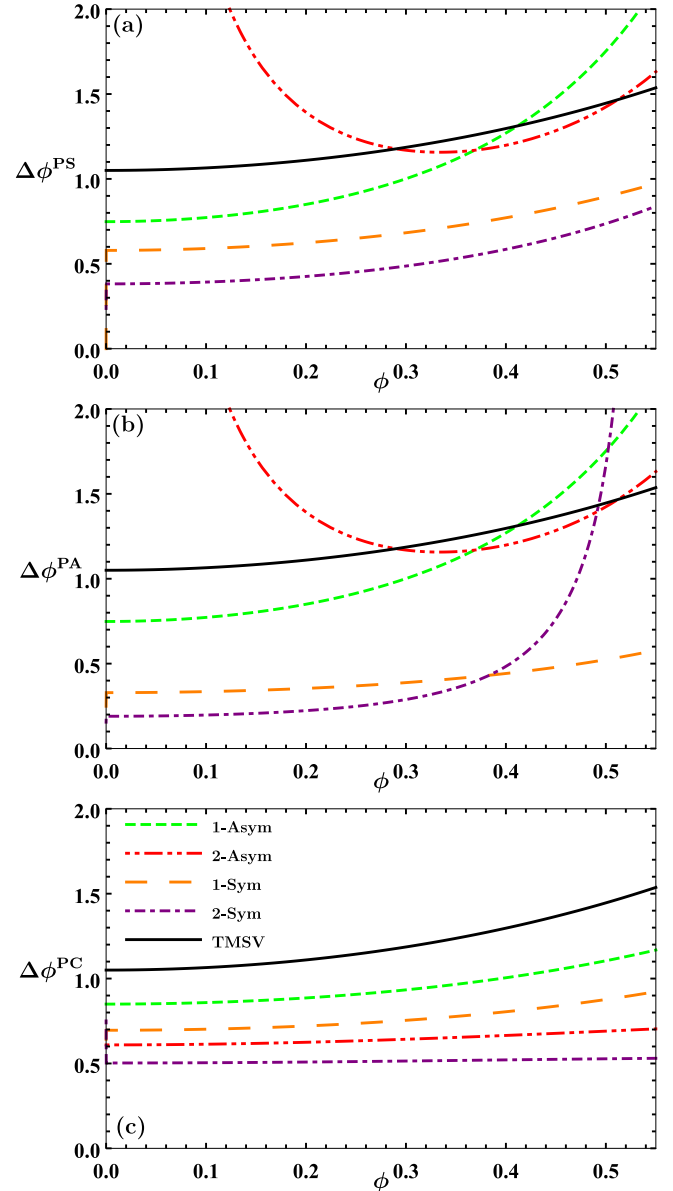
states. These two states do not appear in the graph because their phase sensitivities lie far above the plot range.

In Fig. 8, we show the plot of $\Delta\phi$ as a function of phase for fixed transmissivity and squeezing. We observe that photon catalysis enhances the phase sensitivity even for larger ϕ. Crossover between different PSTMSV and PATMSV states happens for larger values of phase; for instance, the Sym 2-PATMSV state crosses over the Sym 1-PATMSV state at $\phi \approx 0.4$. Furthermore, Asym 2-PSTMSV and Asym 2-PATMSV states perform better than TMSV for a brief interval of ϕ.
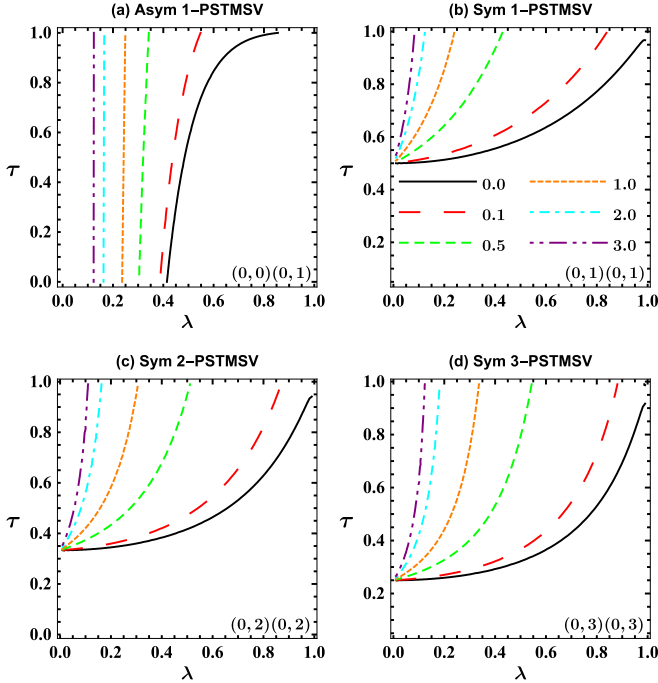
FIG. 9. Plots of fixed $\mathcal{D}^{\mathrm{PS}}$, the difference of $\Delta\phi$ between TMSV and PSTMSV states, as a function of the transmissivity τ and squeezing parameter λ. The value of $(m_1, n_1)(m_2, n_2)$ has been shown in the bottom right. We have set the phase $\phi = 0.01$ rad for all the cases. The labels in panel (b) correspond to plotted values of $\mathcal{D}^{\mathrm{PS}}$. Both the vertical and horizontal axes are dimensionless.

FIG. 10. Plots of fixed $\mathcal{D}^{\mathrm{PA}}$, the difference of $\Delta\phi$ between TMSV and PATMSV states, as a function of the transmissivity τ and squeezing parameter λ. The value of $(m_1, n_1)(m_2, n_2)$ has been shown in the bottom right. We have set the phase $\phi = 0.01$ rad for all the cases. Both the vertical and horizontal axes are dimensionless.

C. Relative performance of NGTMSV states

We now proceed to study the relative performance of the NGTMSV states compared to the TMSV state. To this end, we define a figure of merit, $\mathcal{D}^{\mathrm{NG}}$, as the difference of $\Delta\phi$ between TMSV and NGTMSV states:

$$\mathcal{D}^{\mathrm{NG}} = \Delta\phi^{\mathrm{TMSV}} - \Delta\phi^{\mathrm{NGTMSV}}. \tag{46}$$

This figure of merit enables us to identify the parameter region of transmissivity and squeezing where the NGTMSV states perform better than the TMSV state. This corresponds to the region of a positive $\mathcal{D}^{\mathrm{NG}}$.

We note that the success probability, which represents the fraction of successful non-Gaussian operations per trial, quantifies the resource utilization. We can encounter scenarios where $\mathcal{D}^{\mathrm{NG}}$ is large; however, the success probability is low, representing a poor resource utilization. Therefore, it is better to maximize the product $\mathcal{D}^{\mathrm{NG}} \times P^{\mathrm{NG}}$ rather than $\mathcal{D}^{\mathrm{NG}}$. We first qualitatively take the probabilistic nature into account and then proceed to a quantitative analysis of the same.

We now plot $\mathcal{D}^{\mathrm{NG}}$ for various non-Gaussian states as a function of the transmissivity τ and squeezing parameter λ.

Figure 9 shows the plot of various fixed values of $\mathcal{D}^{\mathrm{PS}}$ (= 0.0, 0.1, 0.5, 1, 2, 3) as a function of the transmissivity τ and squeezing parameter λ. Regions of (τ, λ) with positive values of $\mathcal{D}^{\mathrm{PS}}$ indicate that the PSTMSV states perform better than the TMSV state. The locus of $\mathcal{D}^{\mathrm{PS}} = 0$ progresses along those values of (τ, λ), for which the phase sensitivity of the PSTMSV state is equal to the TMSV state; however, at those specific values of (τ, λ), the PSTMSV state is not the same
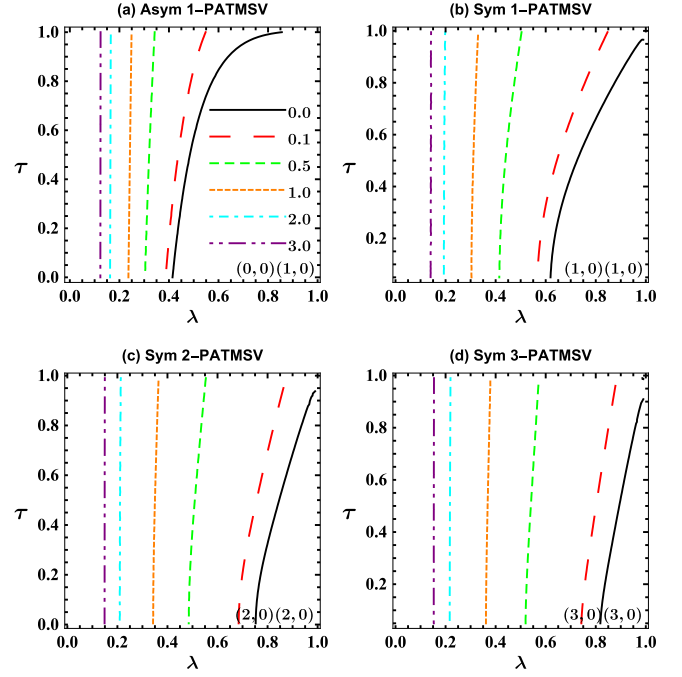
as the TMSV state. The positive region of $\mathcal{D}^{\mathrm{PS}}$ for the Asym 1-PSTMSV state occurs for squeezing below $\lambda \approx 0.4$ for all values of transmissivity. Decreasing the squeezing results in the enhancement of $\mathcal{D}^{\mathrm{PS}}$. However, as we can see from Fig. 2(a), the region of large $\mathcal{D}^{\mathrm{PS}}$ corresponds to a low success probability.

For the Sym 1-PSTMSV state, the region of positive $\mathcal{D}^{\mathrm{PS}}$ lies in a pocket of high transmissivity and low squeezing. As we subtract more photons, the size of the pocket increases. Again, the success probability for the corresponding positive $\mathcal{D}^{\mathrm{PS}}$ region is low.

We can correlate these results with Figs. 6 and 7. For instance, at $\tau = 0.9$, Asym 1-PSTMSV yields a positive $\mathcal{D}^{\mathrm{PS}}$ till $\lambda \approx 0.6$, which corroborates with Fig. 6(a), where the Asym 1-PSTMSV state crosses over the TMSV state at $\lambda \approx 0.6$.

We now plot various fixed values of $\mathcal{D}^{\mathrm{PA}}$ as a function of the transmissivity τ and squeezing parameter λ in Fig. 10. Since the expressions of $\Delta\phi$ for Asym 1-PSTMSV and Asym 1-PATMSV states are the same, the regions of positive $\mathcal{D}^{\mathrm{PS}}$ and $\mathcal{D}^{\mathrm{PA}}$ for these two states coincide. For the Sym 1-PATMSV state, we obtain the positive $\mathcal{D}^{\mathrm{PA}}$ region for even higher values of λ as compared to the Asym 1-PATMSV state. The region is further enlarged for a higher number of symmetric photon subtraction. Furthermore, as we can see from Figs. 2(e)–2(h), the positive $\mathcal{D}^{\mathrm{PA}}$ region overlaps with a high success probability region.

Finally, we plot various fixed values of $\mathcal{D}^{\mathrm{PC}}$ as a function of the transmissivity τ and squeezing parameter λ in Fig. 11. The results show that Asym n-PCTMSV and Sym n-PCTMSV states yield regions with positive $\mathcal{D}^{\mathrm{PC}}$ for all
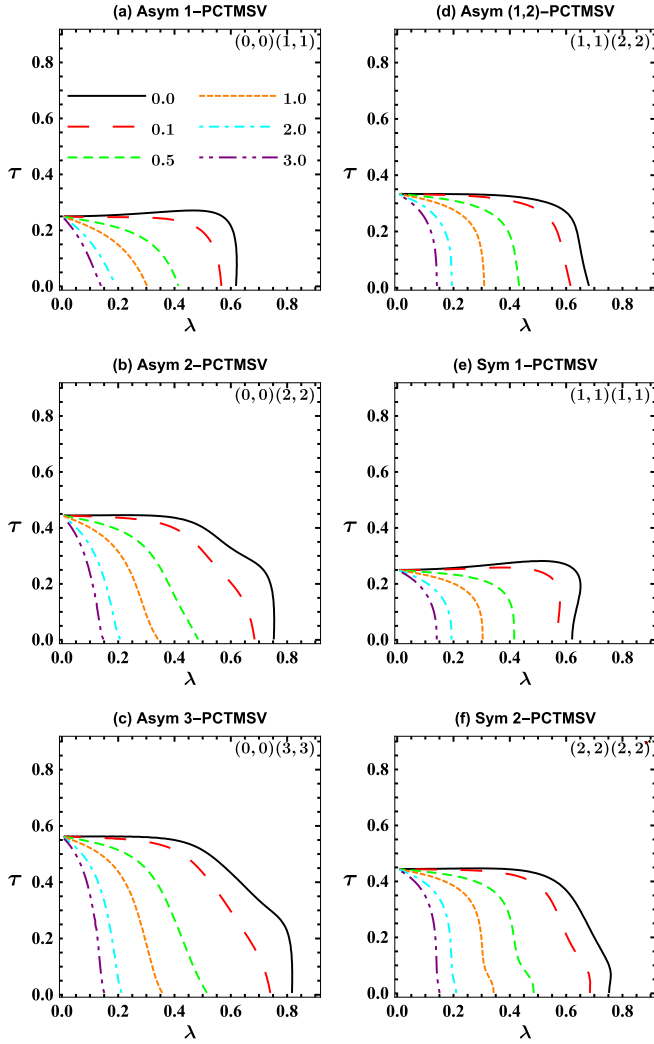
FIG. 11. Plots of fixed $\mathcal{D}^{\mathrm{PC}}$, the difference of $\Delta\phi$ between TMSV and PCTMSV states, as a function of the transmissivity τ and squeezing parameter λ. The value of $(m_1, n_1)(m_2, n_2)$ has been shown in the top right. We have set the phase $\phi = 0.01$ rad for all the cases. Both the vertical and horizontal axes are dimensionless.

values of n. The region of positive $\mathcal{D}^{\mathrm{PC}}$ lies in a pocket of low transmissivity and low squeezing for the Asym 1-PCTMSV and Sym 1-PCTMSV states. As we catalyze more photons asymmetrically and symmetrically, the size of the pocket increases. Here we have also considered the additional case of the Asym (1,2)-PCTMSV state, where the catalysis of one and two photons is performed in modes A_1 and A_2, respectively, which yields a positive result in the low transmissivity and low squeezing regime. The positive $\mathcal{D}^{\mathrm{PC}}$ corresponds to a region of low success probability, as can be seen from Figs. 2(i)–2(l).

Next, we quantitatively take the success probability into account, where we aim to maximize the product $P^{\mathrm{NG}} \times \mathcal{D}^{\mathrm{NG}}$. More specifically, we intend to achieve an optimal tradeoff between P^{NG} and $\mathcal{D}^{\mathrm{NG}}$ by adjusting the transmissivity for a given squeezing.

We compare the value of the product $P^{\mathrm{NG}} \times \mathcal{D}^{\mathrm{NG}}$ for six different non-Gaussian operations, namely, 1-Asym PS,
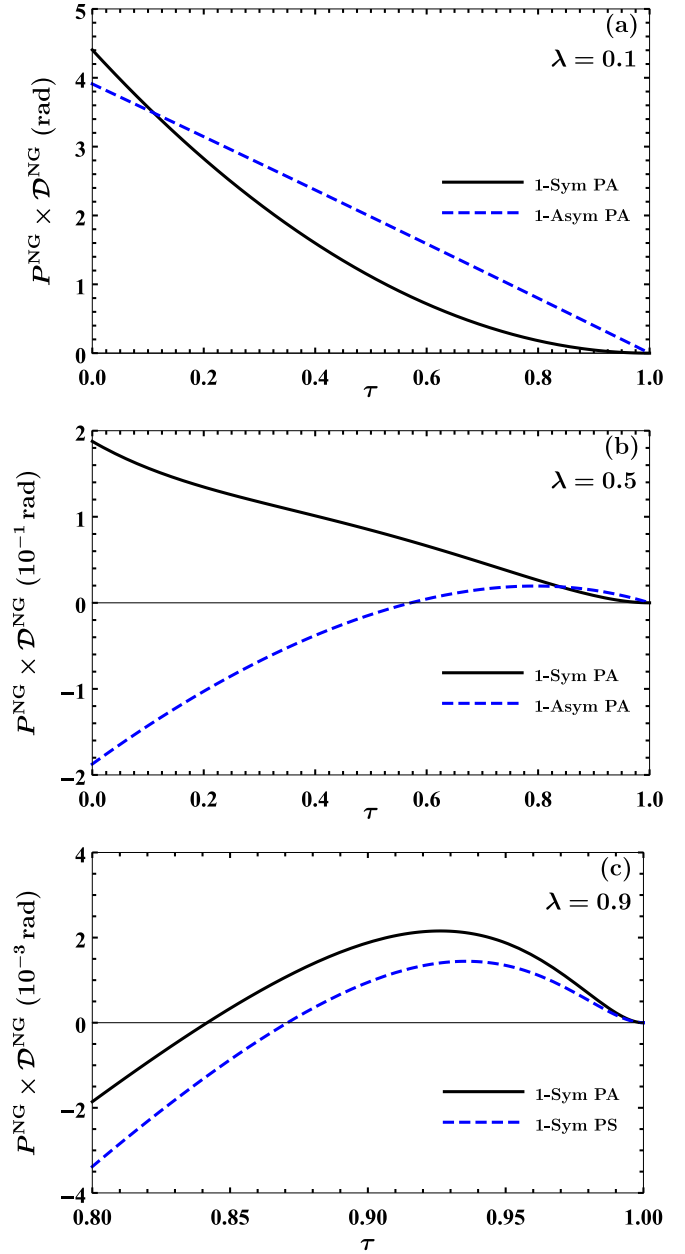

FIG. 12. Plot of $P^{\mathrm{NG}} \times \mathcal{D}^{\mathrm{NG}}$ as a function of the transmissivity τ for different squeezing parameters. We have set the phase $\phi = 0.01$ rad for all the cases.

1-Asym PA, 1-Asym PC, 1-Sym PS, 1-Sym PA, and 1-Sym PC. We plot $P^{\mathrm{NG}} \times \mathcal{D}^{\mathrm{NG}}$ as a function of the transmissivity for different squeezing parameters in Fig. 12. For panels (a) and (b), we have shown only those two curves, which provide maximum advantages for some values of transmissivity, whereas, for panel (c), the curves for the two best performing non-Gaussian operations have been shown. For small squeezing $\lambda = 0.1$, the 1-Sym PA operation outperforms all other operations in small transmissivity regions $0 < \tau < 0.11$, whereas for all other values of transmissivity, the 1-Asym PA operation maximizes the product. For intermediate squeezing $\lambda = 0.5$, 1-Asym PA operation outperforms all other operations in high transmissivity regions $0.84 < \tau < 1$, whereas

for all other values of transmissivity, the 1-Sym PA operation maximizes the product. For high squeezing $\lambda = 0.9$, the 1-Asym PA operation outperforms all other operations in high transmissivity regions $0.84 < \tau < 1$, whereas for all other values of transmissivity, $P^{NG} \times \mathcal{D}^{NG}$ is negative for all non-Gaussian operations, and hence the TMSV state is superior to all other non-Gaussian states considered here.

To conclude this section, the phase sensitivity analysis, along with the success probability consideration, reveals that the photon addition operation is the most advantageous among all the three non-Gaussian operations. Specifically, the 1-Sym PA operation in the low transmissivity and squeezing regime provides maximum advantage.

V. CONCLUSION

In this paper, we derived the generalized Wigner function for non-Gaussian states, including PSTMSV, PATMSV, and PCTMSV states. The free parameters in the Wigner function include the squeezing parameter of the TMSV state and the transmissivity of the beam splitters used to implement the non-Gaussian operations. Further, one can choose the number of photons subtracted, added, or catalyzed on each of the modes of the TMSV state, as per requirement. We then use this generalized Wigner function to calculate the lower bound on the phase sensitivity via QCRB and parity-detection-based phase sensitivity in the MZI.

We have considered a realistic photon subtraction and addition model, which yields the ideal case of photon subtraction and addition in the unit transmissivity limit. Therefore, the phase sensitivity results of ideal symmetric photon subtraction

and addition [38,40], as well as that of asymmetric catalysis [41], on the TMSV state form a particular case of our paper.

We also define a figure of merit as the difference between the phase sensitivity of the TMSV state and the NGTMSV state, which enables us to identify the beneficial squeezing and transmissivity parameter range. Taking the success probability of non-Gaussian state generation into account, it turns out that the photon addition is the most useful operation among all three non-Gaussian operations.

The current paper clearly emphasizes the importance of the probabilistic nature of non-Gaussian state production in the phase sensitivity analysis. We discuss several avenues of future investigations briefly. As we have shown that multiphoton asymmetric subtraction and addition do not provide any advantage over the TMSV state in phase estimation, it would be interesting to explore whether another measurement such as intensity difference in the two output modes of the MZI improves the phase sensitivity for such states. The probabilistic nature of non-Gaussian operations should be considered while studying the effects of different measurements on phase sensitivity. We have considered the implementation of photon addition using a beam splitter, which requires on-demand single-photon sources. Experimentally, photon addition is implemented using parametric down-conversion [53,54], and therefore it is of immense importance to analyze the phase sensitivity in the parametric down-conversion-based photon addition model.

APPENDIX A: EXPLICIT FORM OF THE MATRICES IN THE WIGNER FUNCTION OF THE NGTMSV STATE

Here we provide the explicit form of the matrices M_1, M_2, and M_3 which appear in the Wigner function of the NGTMSV state (21). The matrix M_1 is given by

$$M_1 = \frac{-1}{a_0}\begin{pmatrix} \alpha^2(t_1^2 t_2^2 + 1) + 1 & 0 & -2\alpha\beta t_1 t_2 & 0 \\ 0 & \alpha^2(t_1^2 t_2^2 + 1) + 1 & 0 & 2\alpha\beta t_1 t_2 \\ -2\alpha\beta t_1 t_2 & 0 & \alpha^2(t_1^2 t_2^2 + 1) + 1 & 0 \\ 0 & 2\alpha\beta t_1 t_2 & 0 & \alpha^2(t_1^2 t_2^2 + 1) + 1 \end{pmatrix}, \tag{A1}$$

where $t_i = \sqrt{\tau_i}$ and $r_i = \sqrt{1 - \tau_i}$ ($i = 1, 2$). Further, $\alpha = \sinh r$ and $\beta = \cosh r$. The matrix M_2 is given by

$$M_2 = \frac{-1}{a_0}\begin{pmatrix} -\beta^2 r_1 & -i\beta^2 r_1 & \alpha\beta r_1 t_1 t_2 & -i\alpha\beta r_1 t_1 t_2 \\ \beta^2 r_1 & -i\beta^2 r_1 & -\alpha\beta r_1 t_1 t_2 & -i\alpha\beta r_1 t_1 t_2 \\ \alpha\beta r_2 t_1 t_2 & -i\alpha\beta r_2 t_1 t_2 & -\beta^2 r_2 & -i\beta^2 r_2 \\ -\alpha\beta r_2 t_1 t_2 & -i\alpha\beta r_2 t_1 t_2 & \beta^2 r_2 & -i\beta^2 r_2 \\ -\alpha^2 r_1 t_1 t_2^2 & -i\alpha^2 r_1 t_1 t_2^2 & \alpha\beta r_1 t_2 & -i\alpha\beta r_1 t_2 \\ \alpha^2 r_1 t_1 t_2^2 & -i\alpha^2 r_1 t_1 t_2^2 & -\alpha\beta r_1 t_2 & -i\alpha\beta r_1 t_2 \\ \alpha\beta r_2 t_1 & -i\alpha\beta r_2 t_1 & -\alpha^2 r_2 t_1^2 t_2 & -i\alpha^2 r_2 t_1^2 t_2 \\ -\alpha\beta r_2 t_1 & -i\alpha\beta r_2 t_1 & \alpha^2 r_2 t_1^2 t_2 & -i\alpha^2 r_2 t_1^2 t_2 \end{pmatrix}. \tag{A2}$$

The matrix M_3 is given by

$$
M_3 = \frac{-1}{4a_0}
\begin{pmatrix}
0 & -\beta^2 r_1^2 & -\alpha\beta r_1 r_2 t_1 t_2 & 0 & 0 & \alpha^2 r_2^2 t_1 + t_1 & -\alpha\beta r_1 r_2 t_1 & 0 \\
-\beta^2 r_1^2 & 0 & 0 & -\alpha\beta r_1 r_2 t_1 t_2 & \alpha^2 r_2^2 t_1 + t_1 & 0 & 0 & -\alpha\beta r_1 r_2 t_1 \\
-\alpha\beta r_1 r_2 t_1 t_2 & 0 & 0 & -\beta^2 r_2^2 & -\alpha\beta r_1 r_2 t_2 & 0 & 0 & \alpha^2 r_1^2 t_2 + t_2 \\
0 & -\alpha\beta r_1 r_2 t_1 t_2 & -\beta^2 r_2^2 & 0 & 0 & -\alpha\beta r_1 r_2 t_2 & \alpha^2 r_1^2 t_2 + t_2 & 0 \\
0 & \alpha^2 r_2^2 t_1 + t_1 & -\alpha\beta r_1 r_2 t_2 & 0 & 0 & -\alpha^2 r_1^2 t_2^2 & -\alpha\beta r_1 r_2 & 0 \\
\alpha^2 r_2^2 t_1 + t_1 & 0 & 0 & -\alpha\beta r_1 r_2 t_2 & -\alpha^2 r_1^2 t_2^2 & 0 & 0 & -\alpha\beta r_1 r_2 \\
-\alpha\beta r_1 r_2 t_1 & 0 & 0 & \alpha^2 r_1^2 t_2 + t_2 & -\alpha\beta r_1 r_2 & 0 & 0 & -\alpha^2 r_2^2 t_1^2 \\
0 & -\alpha\beta r_1 r_2 t_1 & \alpha^2 r_1^2 t_2 + t_2 & 0 & 0 & -\alpha\beta r_1 r_2 & -\alpha^2 r_2^2 t_1^2 & 0
\end{pmatrix}.
\tag{A3}
$$

APPENDIX B: EXPLICIT FORM OF THE MATRIX IN THE PROBABILITY EXPRESSION

The matrix M_4 appearing in the success probability expression (24) is given by

$$
M_4 = \frac{-1}{4a_0}
\begin{pmatrix}
0 & \beta^2 r_1^2 & -\alpha\beta r_1 r_2 t_1 t_2 & 0 & 0 & \alpha^2 r_2^2 t_1 + t_1 & \alpha\beta r_1 r_2 t_1 & 0 \\
\beta^2 r_1^2 & 0 & 0 & -\alpha\beta r_1 r_2 t_1 t_2 & \alpha^2 r_2^2 t_1 + t_1 & 0 & 0 & \alpha\beta r_1 r_2 t_1 \\
-\alpha\beta r_1 r_2 t_1 t_2 & 0 & 0 & \beta^2 r_2^2 & \alpha\beta r_1 r_2 t_2 & 0 & 0 & \alpha^2 r_1^2 t_2 + t_2 \\
0 & -\alpha\beta r_1 r_2 t_1 t_2 & \beta^2 r_2^2 & 0 & 0 & \alpha\beta r_1 r_2 t_2 & \alpha^2 r_1^2 t_2 + t_2 & 0 \\
0 & \alpha^2 r_2^2 t_1 + t_1 & \alpha\beta r_1 r_2 t_2 & 0 & 0 & \alpha^2 r_1^2 t_2^2 & -\alpha\beta r_1 r_2 & 0 \\
\alpha^2 r_2^2 t_1 + t_1 & 0 & 0 & \alpha\beta r_1 r_2 t_2 & \alpha^2 r_1^2 t_2^2 & 0 & 0 & -\alpha\beta r_1 r_2 \\
\alpha\beta r_1 r_2 t_1 & 0 & 0 & \alpha^2 r_1^2 t_2 + t_2 & -\alpha\beta r_1 r_2 & 0 & 0 & \alpha^2 r_2^2 t_1^2 \\
0 & \alpha\beta r_1 r_2 t_1 & \alpha^2 r_1^2 t_2 + t_2 & 0 & 0 & -\alpha\beta r_1 r_2 & \alpha^2 r_2^2 t_1^2 & 0
\end{pmatrix}.
\tag{B1}
$$

APPENDIX C: EXPLICIT FORM OF THE MATRICES IN THE MOMENT GENERATING FUNCTION

The matrix M_4 arising in the expression of the moment generating function (29) has already been given in Eq. (B1); we now provide the matrices M_5 and M_6:

$$
M_5 = \frac{-1}{2a_0}
\begin{pmatrix}
-\beta^2 r_1 & -i\beta^2 r_1 & -\alpha\beta r_1 t_1 t_2 & i\alpha\beta r_1 t_1 t_2 \\
\beta^2 r_1 & -i\beta^2 r_1 & \alpha\beta r_1 t_1 t_2 & i\alpha\beta r_1 t_1 t_2 \\
-\alpha\beta r_2 t_1 t_2 & i\alpha\beta r_2 t_1 t_2 & -\beta^2 r_2 & -i\beta^2 r_2 \\
\alpha\beta r_2 t_1 t_2 & i\alpha\beta r_2 t_1 t_2 & \beta^2 r_2 & -i\beta^2 r_2 \\
\alpha^2 r_1 t_1 t_2^2 & i\alpha^2 r_1 t_1 t_2^2 & \alpha\beta r_1 t_2 & -i\alpha\beta r_1 t_2 \\
-\alpha^2 r_1 t_1 t_2^2 & i\alpha^2 r_1 t_1 t_2^2 & -\alpha\beta r_1 t_2 & -i\alpha\beta r_1 t_2 \\
\alpha\beta r_2 t_1 & -i\alpha\beta r_2 t_1 & \alpha^2 r_2 t_1^2 t_2 & i\alpha^2 r_2 t_1^2 t_2 \\
-\alpha\beta r_2 t_1 & -i\alpha\beta r_2 t_1 & -\alpha^2 r_2 t_1^2 t_2 & i\alpha^2 r_2 t_1^2 t_2
\end{pmatrix}
\tag{C1}
$$

and

$$
M_6 = \frac{1}{4a_0}
\begin{pmatrix}
\alpha^2 (t_1^2 t_2^2 + 1) + 1 & 0 & 2\alpha\beta t_1 t_2 & 0 \\
0 & \alpha^2 (t_1^2 t_2^2 + 1) + 1 & 0 & -2\alpha\beta t_1 t_2 \\
2\alpha\beta t_1 t_2 & 0 & \alpha^2 (t_1^2 t_2^2 + 1) + 1 & 0 \\
0 & -2\alpha\beta t_1 t_2 & 0 & \alpha^2 (t_1^2 t_2^2 + 1) + 1
\end{pmatrix}.
\tag{C2}
$$

APPENDIX D: MATRIX IN THE EXPECTATION OF THE PARITY OPERATOR

The matrix M_7 appearing in the average of the parity operator (44) is given by

$$
M_7 = \frac{-1}{4w_0}
\begin{pmatrix}
w_1 & w_2 & w_3 & w_4 & w_5 & w_6 & w_7 & w_8 \\
w_2 & w_1 & w_4 & w_3 & w_6 & w_5 & w_8 & w_7 \\
w_3 & w_4 & w_9 & w_{10} & w_{11} & w_{12} & w_{13} & w_{14} \\
w_4 & w_3 & w_{10} & w_9 & w_{12} & w_{11} & w_{14} & w_{13} \\
w_5 & w_6 & w_{11} & w_{12} & w_{15} & w_{16} & w_{17} & w_{18} \\
w_6 & w_5 & w_{12} & w_{11} & w_{16} & w_{15} & w_{18} & w_{17} \\
w_7 & w_8 & w_{13} & w_{14} & w_{17} & w_{18} & w_{19} & w_{20} \\
w_8 & w_7 & w_{14} & w_{13} & w_{18} & w_{17} & w_{20} & w_{19}
\end{pmatrix},
\tag{D1}
$$

where

$$
\begin{aligned}
w_0 &= 2c_2\lambda^2 t_1^2 t_2^2 + \lambda^4 t_1^4 t_2^4 + 1, & w_{11} &= -c_1\lambda r_1 r_2 t_2\left(\lambda^2 t_1^2 t_2^2 + 1\right), \\
w_1 &= \lambda r_1^2 s_2 t_1 t_2, & w_{12} &= -2c_1\lambda^2 r_1 r_2 s_1 t_1 t_2^2, \\
w_2 &= c_1 r_1^2\left(\lambda^2 t_1^2 t_2^2 + 1\right), & w_{13} &= \lambda r_2^2 s_1 t_1\left(\lambda^2 t_1^2 t_2^2 - 1\right), \\
w_3 &= \lambda r_1 r_2 t_1 t_2\left(c_2 + \lambda^2 t_1^2 t_2^2\right), & w_{14} &= \lambda^2 t_1^2 t_2^3\left(c_2 + \lambda^2 t_1^2\right) + c_2\lambda^2 t_1^2 t_2 + t_2, \\
w_4 &= r_1 r_2 s_1\left(\lambda^2 t_1^2 t_2^2 - 1\right), & w_{15} &= -\lambda^3 r_1^2 s_2 t_1 t_2^3, \\
w_5 &= \lambda r_1^2 s_1 t_2\left(\lambda^2 t_1^2 t_2^2 - 1\right), & w_{16} &= -c_1\lambda^2 r_1^2 t_2^2\left(\lambda^2 t_1^2 t_2^2 + 1\right), \\
w_6 &= \lambda^2 t_2^2 t_1^3\left(c_2 + \lambda^2 t_2^2\right) + c_2\lambda^2 t_2^2 t_1 + t_1, & w_{17} &= -\lambda r_1 r_2\left(c_2\lambda^2 t_1^2 t_2^2 + 1\right), \\
w_7 &= c_1\lambda r_1 r_2 t_1\left(\lambda^2 t_1^2 t_2^2 + 1\right), & w_{18} &= \lambda^2 r_1 r_2 s_1 t_1 t_2\left(\lambda^2 t_1^2 t_2^2 - 1\right), \\
w_8 &= 2c_1\lambda^2 r_1 r_2 s_1 t_1^2 t_2, & w_{19} &= \lambda^3 r_2^2 s_2 t_1^3 t_2, \\
w_9 &= -2c_1\lambda r_2^2 s_1 t_1 t_2, & w_{20} &= c_1\lambda^2 r_2^2 t_1^2\left(\lambda^2 t_1^2 t_2^2 + 1\right), \\
w_{10} &= -c_1 r_2^2\left(\lambda^2 t_1^2 t_2^2 + 1\right),
\end{aligned}
\tag{D2}
$$

with $c_1 = \cos\phi$, $s_1 = \sin\phi$, $c_2 = \cos(2\phi)$, and $s_2 = \sin(2\phi)$.

---

[1] J. P. Dowling, Contemp. Phys. **49**, 125 (2008).

[2] V. Giovannetti, S. Lloyd, and L. Maccone, Nat. Photonics **5**, 222 (2011).

[3] C. M. Caves, Phys. Rev. D **23**, 1693 (1981).

[4] H. Kwon, K. C. Tan, T. Volkoff, and H. Jeong, Phys. Rev. Lett. **122**, 040503 (2019).

[5] H. F. Hofmann and T. Ono, Phys. Rev. A **76**, 031806(R) (2007).

[6] P. M. Anisimov, G. M. Raterman, A. Chiruvelli, W. N. Plick, S. D. Huver, H. Lee, and J. P. Dowling, Phys. Rev. Lett. **104**, 103602 (2010).

[7] V. Giovannetti, S. Lloyd, and L. Maccone, Science **306**, 1330 (2004).

[8] C. C. Gerry, Phys. Rev. A **61**, 043811 (2000).

[9] C. C. Gerry and R. A. Campos, Phys. Rev. A **64**, 063814 (2001).

[10] C. C. Gerry and A. Benmoussa, Phys. Rev. A **65**, 033822 (2002).

[11] R. A. Campos, C. C. Gerry, and A. Benmoussa, Phys. Rev. A **68**, 023810 (2003).

[12] C. C. Gerry and J. Mimih, Phys. Rev. A **82**, 013831 (2010).

[13] C. C. Gerry and J. Mimih, Contemp. Phys. **51**, 497 (2010).

[14] J. Joo, W. J. Munro, and T. P. Spiller, Phys. Rev. Lett. **107**, 083601 (2011).

[15] K. P. Seshadreesan, P. M. Anisimov, H. Lee, and J. P. Dowling, New J. Phys. **13**, 083026 (2011).

[16] W. N. Plick, P. M. Anisimov, J. P. Dowling, H. Lee, and G. S. Agarwal, New J. Phys. **12**, 113025 (2010).

[17] A. Chiruvelli and H. Lee, J. Mod. Opt. **58**, 945 (2011).

[18] K. P. Seshadreesan, S. Kim, J. P. Dowling, and H. Lee, Phys. Rev. A **87**, 043833 (2013).

[19] J. Sahota and D. F. V. James, Phys. Rev. A **88**, 063820 (2013).

[20] X.-X. Zhang, Y.-X. Yang, and X.-B. Wang, Phys. Rev. A **88**, 013838 (2013).

[21] S. D. Huver, C. F. Wildfeuer, and J. P. Dowling, Phys. Rev. A **78**, 063828 (2008).

[22] H. Vahlbruch, M. Mehmet, K. Danzmann, and R. Schnabel, Phys. Rev. Lett. **117**, 110801 (2016).

[23] T. Opatrný, G. Kurizki, and D.-G. Welsch, Phys. Rev. A **61**, 032302 (2000).

[24] Y. Yang and F.-L. Li, Phys. Rev. A **80**, 022315 (2009).

[25] X.-X. Xu, Phys. Rev. A **92**, 012318 (2015).

[26] L. Hu, Z. Liao, and M. S. Zubairy, Phys. Rev. A **95**, 012310 (2017).

[27] S. Wang, L.-L. Hou, X.-F. Chen, and X.-F. Xu, Phys. Rev. A **91**, 063832 (2015).

[28] P. Huang, G. He, J. Fang, and G. Zeng, Phys. Rev. A **87**, 012317 (2013).

[29] H.-X. Ma, P. Huang, D.-Y. Bai, S.-Y. Wang, W.-S. Bao, and G.-H. Zeng, Phys. Rev. A **97**, 042329 (2018).

[30] Y. Guo, W. Ye, H. Zhong, and Q. Liao, Phys. Rev. A **99**, 032327 (2019).

[31] W. Ye, H. Zhong, Q. Liao, D. Huang, L. Hu, and Y. Guo, Opt. Express **27**, 17186 (2019).

[32] C. Kumar, J. Singh, S. Bose, and Arvind, Phys. Rev. A **100**, 052329 (2019).

[33] L. Hu, M. Al-amri, Z. Liao, and M. S. Zubairy, Phys. Rev. A **102**, 012608 (2020).

[34] S.-H. Tan, B. I. Erkmen, V. Giovannetti, S. Guha, S. Lloyd, L. Maccone, S. Pirandola, and J. H. Shapiro, Phys. Rev. Lett. **101**, 253601 (2008).

[35] E. D. Lopaeva, I. Ruo Berchera, I. P. Degiovanni, S. Olivares, G. Brida, and M. Genovese, Phys. Rev. Lett. **110**, 153603 (2013).

[36] S. Zhang and X. Zhang, Phys. Rev. A **97**, 043830 (2018).

[37] R. Birrittella, J. Mimih, and C. C. Gerry, Phys. Rev. A **86**, 063828 (2012).

[38] R. Carranza and C. C. Gerry, J. Opt. Soc. Am. B **29**, 2581 (2012).

[39] D. Braun, P. Jian, O. Pinel, and N. Treps, Phys. Rev. A **90**, 013821 (2014).

[40] Y. Ouyang, S. Wang, and L. Zhang, J. Opt. Soc. Am. B **33**, 1373 (2016).

[41] H. Zhang, W. Ye, C. Wei, Y. Xia, S. Chang, Z. Liao, and L. Hu, Phys. Rev. A **103**, 013705 (2021).

[42] T. J. Bartley and I. A. Walmsley, New J. Phys. **17**, 023038 (2015).

[43] Arvind, B. Dutta, N. Mukunda, and R. Simon, Pramana **45**, 471 (1995).

[44] S. L. Braunstein and P. van Loock, Rev. Mod. Phys. **77**, 513 (2005).

[45] G. Adesso and F. Illuminati, J. Phys. A: Math. Theor. **40**, 7821 (2007).

[46] C. Weedbrook, S. Pirandola, R. García-Patrón, N. J. Cerf, T. C. Ralph, J. H. Shapiro, and S. Lloyd, Rev. Mod. Phys. **84**, 621 (2012).

[47] G. Adesso, S. Ragy, and A. R. Lee, Open Syst. Inf. Dyn. **21**, 1440001 (2014).

[48] A. Royer, Phys. Rev. A **15**, 449 (1977).

[49] B. Yurke, S. L. McCall, and J. R. Klauder, Phys. Rev. A **33**, 4033 (1986).

[50] S. L. Braunstein and C. M. Caves, Phys. Rev. Lett. **72**, 3439 (1994).

[51] M. Jarzyna and R. Demkowicz-Dobrzański, Phys. Rev. A **85**, 011801(R) (2012).

[52] R. J. Birrittella, P. M. Alsing, and C. C. Gerry, AVS Quantum Science **3**, 014701 (2021).

[53] A. Zavatta, S. Viciani, and M. Bellini, Science **306**, 660 (2004).

[54] A. Zavatta, V. Parigi, and M. Bellini, Phys. Rev. A **75**, 052106 (2007).